

Stepwise Positional-Orientational Order and the Multicritical-Multistructural Global Phase Diagram of the $s = 3/2$ Ising Model from Renormalization-Group Theory

Çağın Yunus¹, Başak Renklioğlu^{2,3}, Mustafa Keskin⁴, and A. Nihat Berker^{5,6}

¹*Department of Physics, Boğaziçi University, Bebek 34342, Istanbul, Turkey*

²*College of Sciences, Koç University, Sarıyer 34450, Istanbul, Turkey*

³*Department of Physics, Bilkent University, Bilkent 06533, Ankara, Turkey*

⁴*Department of Physics, Erciyes University, Kayseri 38039, Turkey*

⁵*Faculty of Engineering and Natural Sciences, Sabancı University, Tuzla 34956, Istanbul, Turkey and*

⁶*Department of Physics, Massachusetts Institute of Technology, Cambridge, Massachusetts 02139, U.S.A.*

The spin-3/2 Ising model, with nearest-neighbor interactions only, is the prototypical system with two different ordering species, with concentrations regulated by a chemical potential. Its global phase diagram, obtained in $d = 3$ by renormalization-group theory in the Migdal-Kadanoff approximation or equivalently as an exact solution of a $d = 3$ hierarchical lattice, with flows subtended by 40 different fixed points, presents a very rich structure containing eight different ordered and disordered phases, with more than fourteen different types of phase diagrams in temperature and chemical potential. It exhibits phases with orientational and/or positional order. It also exhibits quintuple phase transition reentrances. Universality of critical exponents is conserved across different renormalization-group flow basins, via redundant fixed points. One of the phase diagrams contains a plastic crystal sequence, with positional and orientational ordering encountered consecutively as temperature is lowered. The global phase diagram also contains double critical points, first-order and critical lines between two ordered phases, critical endpoints, usual and unusual (inverted) bicritical points, tricritical points, multiple tetracritical points, and zero-temperature criticality and bicriticality. The 4-state Potts permutation-symmetric subspace is contained in this model.

PACS numbers: 64.60.Cn, 05.50.+q, 61.43.-j, 75.10.Hk

I. INTRODUCTION

The spin-3/2 Ising model, with nearest-neighbor interactions only, exhibits intricate but physically suggestive phase diagrams, as for example shown in Fig. 1(f) including three separate ferromagnetic phases and an only positionally ordered phase, new special points, a conservancy of the universality principle of critical exponents via the redundant fixed-point mechanism, and a temperature sequence of stepwise positional and orientational ordering as in plastic crystals. Other phase diagram cross-sections of the global phase diagram, with eight different ordered and disordered phases, include order-order double critical points, first-order and critical lines between ordered phases, critical endpoints, usual and unusual (inverted) bicritical points, tricritical points, different types of tetracritical points, and zero-temperature criticality and bicriticality. The permutation-symmetric 4-state Potts subspace is lodged in this model.

The Hamiltonian of the spin-1/2 Ising model, $-\beta\mathcal{H} = \sum_{\langle ij \rangle} J s_i s_j$, where at each site i there is a spin $s_i = \pm 1$ and the sum is over all pairs of nearest-neighbor sites, generalizes for the spin-1 Ising model to

$$-\beta\mathcal{H} = \sum_{\langle ij \rangle} [J s_i s_j + K s_i^2 s_j^2 - \Delta(s_i^2 + s_j^2)], \quad (1)$$

where $s_i = \pm 1, 0$. [1] Eq.(1) constitutes the most general spin-1 Ising model with nearest-neighbor interactions only and no externally imposed symmetry breaking in the ordering degrees of freedom. The global understanding [2, 3] of the phase diagram of the spin-1 Ising model played an important role through applicability to many

physical systems that incorporate non-ordering degrees of freedom ($s_i = 0$) as well as ordering degrees of freedom ($s_i = \pm 1$). The next qualitative step is the global study of a model that has two different types of local ordering degrees of freedom, namely the spin-3/2 Ising model [4–29]:

$$-\beta\mathcal{H} = \sum_{\langle ij \rangle} [(J_1 P_i P_j + J_{13}(P_i Q_j + Q_i P_j) + J_3 Q_i Q_j) s_i s_j + (K_1 P_i P_j + K_{13}(P_i Q_j + Q_i P_j) + K_3 Q_i Q_j) s_i^2 s_j^2 - \Delta(s_i^2 + s_j^2)], \quad (2)$$

where $s_i = \pm 3/2, \pm 1/2$, is the most general spin-3/2 Ising model with only nearest-neighbor interactions and no externally imposed symmetry breaking in the ordering degrees of freedom. The projection operators in Eq.(2) are $P_i = 1 - Q_i = 1(0)$ for $s_i = \pm 1/2(\pm 3/2)$.

Of the models defined above, the spin-1/2 Ising model has a single critical point on the temperature J^{-1} axis. The spin-1 Ising model, in the temperature and chemical potential Δ/J plane, has three different types of phase diagrams when the biquadratic interaction K is non-negative.[2] When negative biquadratic interactions are considered, nine different types of phase diagrams are obtained from mean-field theory.[3] We find in our current work on the spin-3/2 Ising model, using renormalization-group theory, an extraordinarily rich solution, with numerous types of phase diagrams in temperature and chemical potential, exhibiting first- and second-order phase transitions between eight different variously ordered and disordered phases.

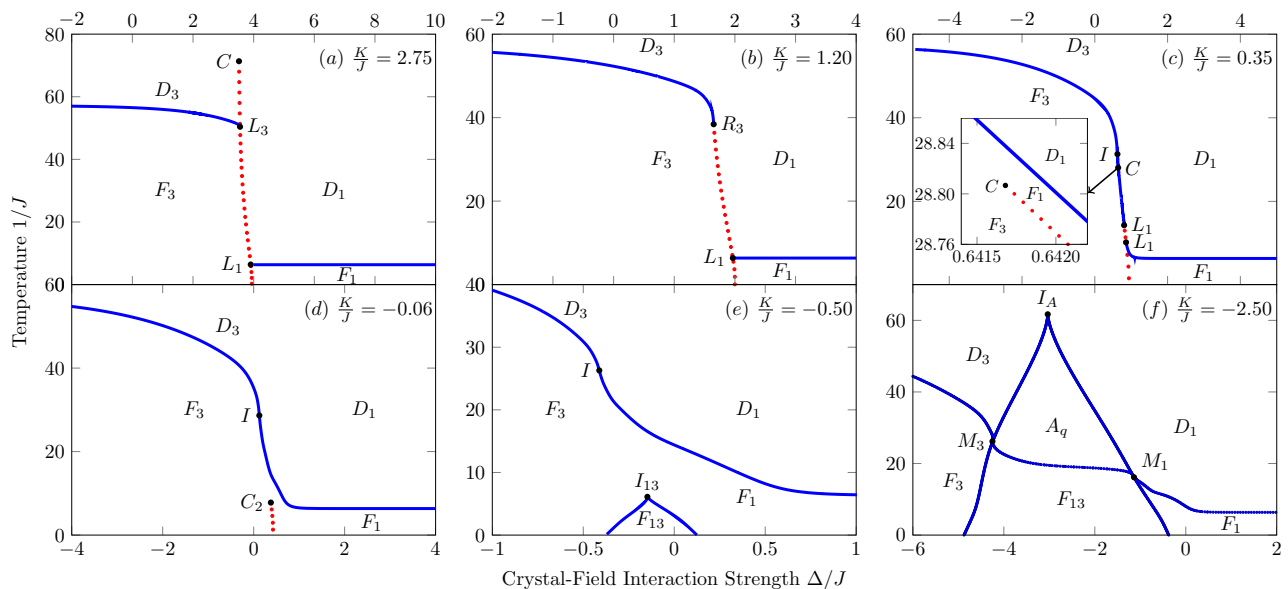


FIG. 1: (Color online) Temperature versus chemical potential phase diagrams of the spin-3/2 Ising model for $d = 3$, for (a) $K/J = 2.75$, (b) $K/J = 1.20$, (c) $K/J = 0.35$, (d) $K/J = 0.06$, (e) $K/J = -0.50$, (f) $K/J = -2.50$. The first- and second-order phase transitions are drawn with dotted and full curves, respectively. The phases F_1 and F_3 are ferromagnetically ordered with predominantly $|s| = 1/2$ and $|s| = 3/2$, respectively. The phases D_1 and D_3 are disordered with predominantly $|s| = 1/2$ and $|s| = 3/2$, respectively. The phase F_{13} is positionally and ferromagnetically ordered and the phase A_q is positionally ordered and magnetically disordered. The point C is an ordinary critical point and the point C_2 is a double critical point. The points L_1 and L_3 are critical endpoints. The point R_3 is a tricritical point. The points M_1 and M_3 are tetracritical points. The points I , I_{13} , and I_A each separate two segments of second-order phase transitions, between the same two phases, where in spite of renormalization-group flows to different basins, critical exponent universality is sustained via redundant fixed points.

The Hamiltonian of Eq.(2) is expressed as

$$-\beta\mathcal{H} = \sum_{\langle ij \rangle} [-\beta\mathcal{H}(s_i, s_j)], \quad (3)$$

where the nearest-neighbor Hamiltonian is

$$\begin{aligned} -\beta\mathcal{H}(s_i, s_j) = & [J_1 P_i P_j + J_{13}(P_i Q_j + Q_i P_j) \\ & + J_3 Q_i Q_j] s_i s_j + [K_1 P_i P_j + K_{13}(P_i Q_j + Q_i P_j) \\ & + K_3 Q_i Q_j] s_i^2 s_j^2 - \Delta(s_i^2 + s_j^2). \end{aligned} \quad (4)$$

The transfer matrix, used below, is the exponentiated nearest-neighbor Hamiltonian

$$T(s_i, s_j) = e^{-\beta\mathcal{H}(s_i, s_j)}. \quad (5)$$

We perform the renormalization-group treatment of the system, for spatial dimension d and length-rescaling factor b , using the Migdal-Kadanoff approximation [30, 31] or equivalent exact solution of a $d = 3$ hierarchical lattice [32]. This calculation is effected by taking the b^{d-1} th power of each term of the transfer matrix and then by taking the b th power of the resulting matrix. At each stage, each element of the resulting matrix is divided by the largest element, which is equivalent to subtracting an additive constant from the Hamiltonian. From spin-up-down and nearest-neighbor-interchange symmetries, the transfer matrix has 6 independent matrix elements, namely $(T_{33}, T_{11}, T_{31}, T_{1-1}, T_{3-1}, T_{3-3})$, where the

subscripts refer to the $2s_i, 2s_j$ values), one of which is 1 due to the division mentioned above. Thus, the renormalization-group flows are in 5-dimensional interaction space. These renormalization-group flows are followed until the stable fixed points of the phases or the unstable fixed points of the phase transitions are reached, thereby precisely mapping the global phase diagram from the initial conditions of the variously ending trajectories.[2] Analysis at the unstable fixed points yields the order of the phase transitions and the critical exponents of the second-order transitions. Thus, we have studied the spin-3/2 Ising model in spatial three dimensions $d = 3$ with length rescaling factor $b = 3$, obtaining the global phase diagram, which is underpinned by 40 renormalization-group fixed points (Table I). Similar calculations have been done in $d = 2$ [7, 13] and $d = 3$ [14].

Our renormalization-group treatment constitutes an exact solution for hierarchical lattices [32–37] which are being extensively used [38–72]. Our treatment is simultaneously an approximate solution [30, 31] for hypercubic lattices. This approximation for the cubic lattice is an uncontrolled approximation, as in fact are all renormalization-group theory calculations in $d = 3$ and all mean-field theory calculations. However, the local summation in position-space technique used here has been qualitatively, near-quantitatively, and predictively successful in a large variety of problems, such as

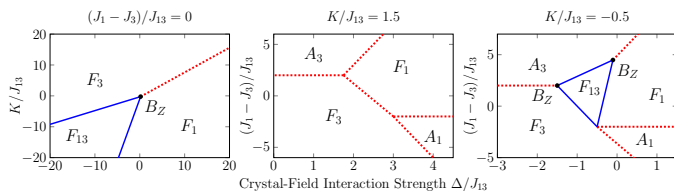


FIG. 2: (Color online) Zero-temperature ($J, J_{13} \rightarrow \infty$) phase diagrams. The first- and zero-temperature second-order phase transitions are drawn with dotted and full curves, respectively. The phases F_1 and F_3 are ferromagnetically ordered with predominantly $|s| = 1/2$ and $|s| = 3/2$, respectively. The phase F_{13} is positionally and ferromagnetically ordered. The phases A_1 and A_3 are antiferromagnetically ordered with predominantly $|s| = 1/2$ and $|s| = 3/2$, respectively. The points B_Z are zero-temperature bicritical points which, being at zero temperature, accommodate boundary lines at finite angles.

arbitrary spin- s Ising models [73], global Blume-Emery-Griffiths model [2], first- and second-order Potts transitions [74, 75], antiferromagnetic Potts critical phases [76, 77], ordering [78] and superfluidity [79] on surfaces, multiply reentrant liquid crystal phases [80, 81], chaotic spin glasses [82], random-field [83] and random-temperature [84] magnets, and high-temperature superconductors [85].

II. GLOBAL PHASE DIAGRAM

We start by studying $J_1 = J_{13} = J_3 \equiv J$ and $K_1 = K_{13} = K_3 \equiv K$. Thus, $1/J$ is proportional to temperature and will be used as our temperature variable. In our system, one of the ordering species is $|s_i| = 3/2$, the other one is $|s_i| = 1/2$. The chemical potential Δ/J (dividing out inverse temperature) controls the relative amounts of each ordering species. The biquadratic interaction K/J (again dividing out inverse temperature) controls the separation/mixing of the two ordering species. Fig. 1 shows the effects of the biquadratic interaction on the global phase diagram.

The temperature versus chemical potential phase diagram for large K/J , where separation is favored, is illustrated in Fig. 1(a) with $K/J = 2.75$. In this phase diagram, two ferromagnetically ordered phases F_3 and F_1 are seen at low temperatures, each rich in one of the ordering species, namely respectively rich in $|s_i| = 3/2$ and $|s_i| = 1/2$. Upon increasing temperature, each ferromagnetic phase undergoes a second-order phase transition to the disordered (paramagnetic) phase that is rich in the corresponding species, respectively D_3 and D_1 . By changing the chemical potential Δ/J , three different first-order phase transitions are induced between phases rich in different species: A four-phase coexistence line between the ferromagnetic phases F_3 and F_1 at low temperatures, a three-phase coexistence line between the ferromagnetic phase F_3 and the disordered phase D_1 at intermediate temperatures, and a two-phase coexistence line

between the disordered phases D_3 and D_1 at high temperatures. Each of the different first-order fixed points are given in Table I. The latter first-order transition terminates at high temperature at the isolated critical point C . At intermediate temperatures, both second-order transition lines terminate on the first-order boundary, at critical endpoints L_3 and L_1 . The corresponding hybrid fixed points, which include both first-order ($y_1 = d$) and second-order ($0 < y_2 < d$) characteristics [2], are given in Table I.

As the biquadratic coupling strength K/J is decreased from large positive values, lessening the tendency of the two ordering species to separate, the first-order phase transition line between their respective disordered phases shrinks, so that the isolated critical point C and the upper critical endpoint L_3 approach each other and merge, to form the tricritical point R_3 . The resulting phase diagram is illustrated in Fig. 1(b) with $K/J = 1.20$.

At lower values of the biquadratic coupling strength K/J , a narrow band of the ferromagnetic F_1 phase appears, decoupled from the main F_1 region, between the F_3 and D_1 regions, as seen in Fig. 1(c) for $K/J = 0.35$. The first-order phase boundary between this narrow F_1 region and the F_3 region extends, at lower temperature, to the upper critical endpoint L_1 and, at higher temperature, to an isolated critical point C_2 as seen in the inset in Fig. 1(c). This isolated critical point, totally imbedded in ferromagnetism, is thus a double critical point [20], as it mediates between the positively magnetized F_3 and F_1 and, separately, between the negatively magnetized F_3 and F_1 . Due to this order-order critical point, it is possible to go continuously, without encountering a phase transition, between the ordered F_3 and F_1 phases. The second-order phase boundary extending to the upper L_1 is composed of two segments, on each side of the point I , separately subtended by the $F_3 - D_3$ and $F_1 - D_1$ critical fixed points. The universality principle of the critical exponents is sustained here by the redundant [86] fixed-point mechanism: Although these two fixed points are globally separated in the renormalization-group flow diagram, they have identical critical exponents (which is furthermore shared by the fixed point of I), as seen in Table I.

At lower values of K/J , the two critical endpoints L_1 merge and annihilate. A single second-order phase boundary, between the F_3 or F_1 ordered phase at low temperature and the D_3 or D_1 disordered phase at high temperature, extends across the entire phase diagram, as seen in Fig. 1(d) for $K/J = -0.06$. The universality principle is sustained along this second-order phase boundary by the redundancy of the fixed points, as explained above. A single first-order boundary forms between the F_3 and F_1 ordered phases, disconnected from the second-order boundary to the D_3 and D_1 disordered phases. This phase diagram, for $d = 3$ from renormalization-group theory, agrees with the phase diagram previously found for $d = 2$ by finite-size scaling and Monte Carlo [10, 11].

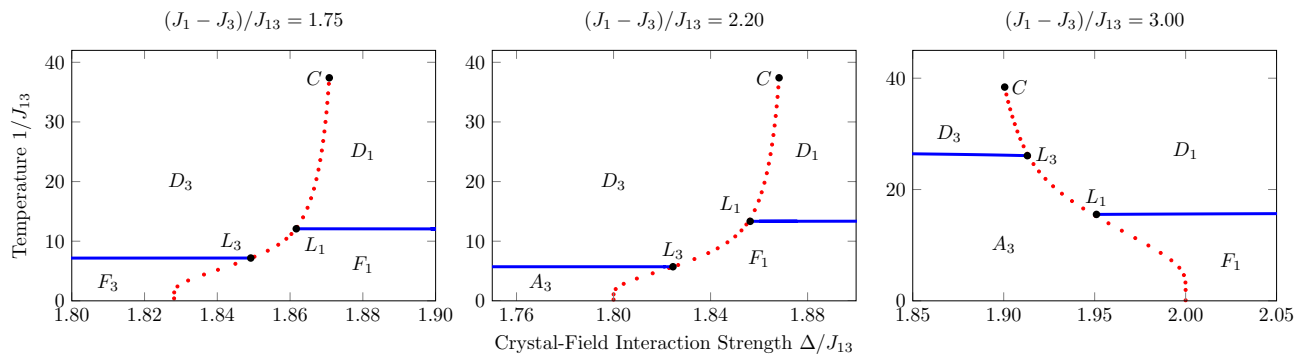


FIG. 3: (Color online) Phase diagrams evolving from the Fig. 1(a) topology, with $K/J_{13} = 1.50$. As $(J_1 - J_3)/J_{13}$ is increased, the second-order transition temperature to the ferromagnetic phase F_3 falls below the second-order transition temperature to the ferromagnetic phase F_1 , as seen for $(J_1 - J_3)/J_{13} = 1.75$. Eventually, the ferromagnetic phase F_3 disappears at zero temperature and an antiferromagnetic phase A_3 , predominantly with $|s_i| = 3/2$, appears from zero temperature, as seen for $(J_1 - J_3)/J_{13} = 2.20$. As $(J_1 - J_3)/J_{13}$ is further increased, the second-order transition temperature to the antiferromagnetic phase A_3 moves above the second-order transition temperature to the ferromagnetic phase F_1 , as seen for $(J_1 - J_3)/J_{13} = 3.00$.

As the biquadratic coupling strength K/J is further decreased, increasing the tendency of the two ordering species to mix, the first-order boundary between F_3 and F_1 shrinks to zero temperature and thus disappears. In fact, ordered mixing appears: A sublattice-wise (i.e., positionally) ordered, as well as magnetically (i.e., orientationally) ordered ferrimagnetic phase F_{13} appears at $K/J \leq -1/4$. In this phase, one of two sublattices is predominantly $|s_i| = 3/2$ and the other sublattice is predominantly $|s_i| = 1/2$, and the system is magnetized. As illustrated in Fig. 1(e) for $K/J = -0.50$, the F_{13} phase occurs at low temperatures and intermediate chemical potentials. The phase boundary between F_{13} and F_3 or F_1 is second-order and remarkably extends to zero-temperature.

For even more negative values of K/J , a portion of the sublattice-ordered phase has erupted through the ferromagnetic ordering lines and in the process lost ferromagnetic ordering, as illustrated in Fig. 1(f) with $K/J = -2.50$. Thus, a new (antiquadrupolar [3]) phase A_q appears, that is sublattice-wise (positionally) ordered, but paramagnetic. Each ordering species predominantly occurs in one of the two sublattices, with no preferred spin orientation. This regime offers a phase diagram topology including four different ordered phases. Two of the ordered phases are orientationally ordered, one phase is positionally ordered, and one phase is both orientationally and positionally ordered. Note that, at intermediate chemical potentials, as temperature is lowered, the sequence of disordered, then only positionally ordered, finally positionally and orientationally ordered phases is encountered, as in plastic crystal systems.[87] Second-order phase transition lines cross at the tetracritical [94] points M_3 and M_1 . Again, no violation of universality is seen around the phase F_{13} in Fig. 1(e) or around the phase A_q in Fig. 1(f), the segments on each side of the points I_{13} and I_A having different fixed points but same critical exponents (Table I). Phase diagrams similar to

Fig. 1(e,f) have been seen by renormalization-group theory in $d = 2, 3$ [7, 13, 14]. The phase diagram sequence in Fig.1 (d-f) is in qualitative topological agreement with Bethe lattice solution [17].

The calculated finite-temperature global phase diagram given in Fig. 1 agrees with the zero-temperature phase diagram given in the left panel of Fig. 2, calculated by ground-state energy crossings. It is seen that the zero-temperature phase diagram includes a zero-temperature bicritical point B_Z at $K/J = -1/4, \Delta/J = 3/16$.

III. DIFFERENTIATED SPECIES COUPLING

The spin-3/2 Ising model carries an even richer structure of phase diagrams, accessed by differentiating the interaction constants in Eq. (2). We give here two sequences of phase diagrams with $J_1 > J_3, J_{13} = (J_1 + J_3)/2$.

A. Phase Diagrams Evolving from the Figure 1(a) Topology

Figure 3 shows phase diagrams with $K/J_{13} = 1.50$. As $(J_1 - J_3)/J_{13}$ is increased, the second-order transition temperature to the ferromagnetic phase F_3 falls below the second-order transition temperature to the ferromagnetic phase F_1 , as seen for $(J_1 - J_3)/J_{13} = 1.75$. Eventually, the ferromagnetic phase F_3 disappears at zero temperature and an antiferromagnetic phase A_3 , predominantly with $|s_i| = 3/2$, appears from zero temperature, as seen for $(J_1 - J_3)/J_{13} = 2.20$. As $(J_1 - J_3)/J_{13}$ is further increased, the second-order transition temperature to the antiferromagnetic phase A_3 moves above the second-order transition temperature to the ferromagnetic phase F_1 , as seen for $(J_1 - J_3)/J_{13} = 3.00$.

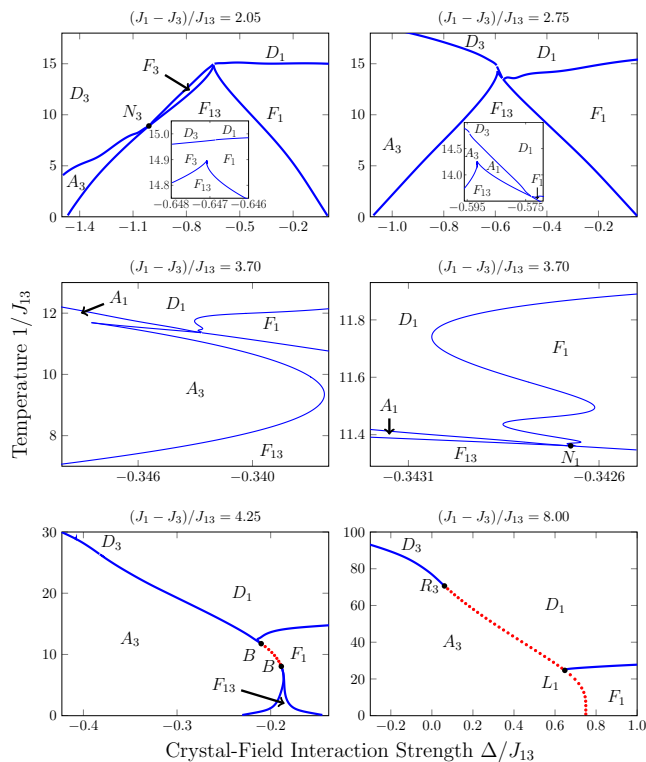


FIG. 4: (Color online) Phase diagrams evolving from the Fig. 1(e) topology, with $K/J_{13} = -0.50$. As $(J_1 - J_3)/J_{13}$ is increased, the second-order transition temperature to the ferromagnetic phase F_3 is depressed and the antiferromagnetic phase A_3 appears for more negative values of the crystal-field interaction Δ/J_{13} , where the spin magnitude $|s_i| = 3/2$ is more favored, as seen for $(J_1 - J_3)/J_{13} = 2.05$. Four second-order phase transition lines meet at the tetracritical point N_3 . The inset shows that the phase diagram topology near the maximal temperatures of the phase F_{13} is yet unaltered from Fig. 1(e). In this phase diagram region, as $(J_1 - J_3)/J_{13}$ is further increased, the phase A_3 replaces F_3 , which is eliminated, as seen for $(J_1 - J_3)/J_{13} = 2.75$. The tetracritical point moves, as N_1 , to the less negative crystal-field side of F_{13} . As seen in the phase diagrams for $(J_1 - J_3)/J_{13} = 3.70$, many phase-transition reentrances occur in the neighborhood of the tetracritical point N_1 : As temperature is lowered, the phase transitions to F_1 are quintuply reentrant. The phase transitions to F_{13} are singly reentrant. It should be noted that our current calculation, showing these complicated multiple reentrances, is exact for the hierarchical lattice with spatial dimension $d = 3$. As $(J_1 - J_3)/J_{13}$ is further increased, the multicritical point N_1 splits into usual and "inverted" bicritical points B connected by a first-order transition line between the antiferromagnetic phase A_3 and the ferromagnetic phase F_1 , as seen for $(J_1 - J_3)/J_{13} = 4.75$. As $(J_1 - J_3)/J_{13}$ is further increased, the higher-temperature bicritical point splits into a tricritical point R_3 and a critical endpoint L_1 and the lower-temperature unusual bicritical point disappears, along with the phase F_{13} , at zero temperature, as seen for $(J_1 - J_3)/J_{13} = 8.00$.

The finite-temperature phase diagrams of Fig. 3 are consistent with the corresponding zero-temperature phase diagram, in the middle panel of Fig. 2. Conversely and not shown here, when $(J_1 - J_3)/J_{13}$ is made negative, an antiferromagnetic phase A_1 , predominantly with $|s_i| = 1/2$, similarly appears, as seen in Fig. 2.

B. Phase Diagrams Evolving from the Figure 1(e) Topology

Figure 4 shows phase diagrams with $K/J_{13} = -0.50$. As $(J_1 - J_3)/J_{13}$ is increased, the second-order transition temperature to the ferromagnetic phase F_3 is depressed and the antiferromagnetic phase A_3 appears for more negative values of the crystal-field interaction Δ/J_{13} , where the spin magnitude $|s_i| = 3/2$ is more favored, as seen for $(J_1 - J_3)/J_{13} = 2.05$. Four second-order phase transition lines meet at the tetracritical point N_3 . The inset shows that the phase diagram topology is unaltered near the maximal temperatures of the phase F_{13} . In this phase diagram region, as $(J_1 - J_3)/J_{13}$ is further increased, A_3 replaces F_3 , which is eliminated, as seen for $(J_1 - J_3)/J_{13} = 2.75$. The tetracritical point moves, as N_1 , to the less negative crystal-field side of F_{13} . As seen in the phase diagrams for $(J_1 - J_3)/J_{13} = 3.70$, many phase transition reentrances [80, 81, 88–92] occur in the neighborhood of the tetracritical point N_1 : As temperature is lowered, the phase transitions to F_1 are quintuply reentrant. The phase transitions to F_{13} are singly reentrant. Previously, up to quadruply reentrant phase transitions have been found for liquid crystal systems [80, 81, 88–91] and surface systems [92]. Much higher reentrances have been calculated in the high- T_C superconductivity tJ model.[93]. It should be noted that our current calculation, showing these complicated reentrances, is exact for the hierarchical lattice with spatial dimension $d = 3$. As $(J_1 - J_3)/J_{13}$ is further increased, the tetracritical point N_1 splits into two bicritical points B connected by a first-order transition line between the antiferromagnetic phase A_3 and the ferromagnetic phase F_1 , as seen in Fig. 4 for $(J_1 - J_3)/J_{13} = 4.75$. At a (non-zero-temperature) bicritical point, normally, two high-temperature second-order boundaries and one low-temperature first-order boundary meet tangentially.[94] In our present phase diagram, the opposite temperature ordering occurs at the lower-temperature bicritical point. Thus, this is an "inverted bicritical point". As $(J_1 - J_3)/J_{13}$ is further increased, the higher-temperature bicritical point splits into a tricritical point R_3 and a critical endpoint L_1 and the lower-temperature inverted bicritical point disappears, along with the phase F_{13} , at zero temperature, as seen in Fig. 4 for $(J_1 - J_3)/J_{13} = 8.00$.

Thus, both multicritical points, bicritical and tetracritical, of the classic coupled-order-parameter problem [94] is contained within the spin-3/2 Ising model. The finite-temperature phase diagrams of Fig. 4 are consis-

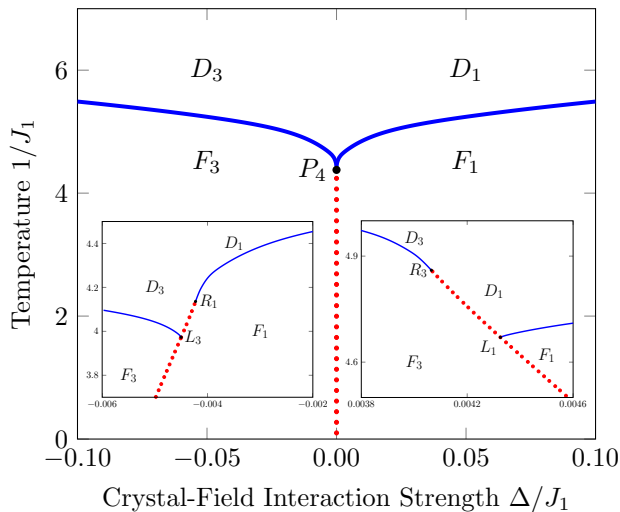


FIG. 5: (Color online) The phase diagram for the 4-state Potts side conditions $4J_1 = 36J_3 = K_1 = 81K_3$, $J_{13} = K_{13} = 0$. In this figure, $\Delta/J_1 = 0$ is the 4-state Potts subspace, where the system is permutation symmetric with respect to the 4 states $s_i = \pm 3/2, \pm 1/2$. Varying Δ/J_1 from zero gives the symmetric bicritical phase diagram around the Potts transition point P_4 . This phase diagram is exact for the $d = 3$ hierarchical lattice, but approximate for the cubic lattice, as explained in the text. Away from the 4-Potts condition, e.g. for $3.5J_1 = 36J_3 = K_1 = 81K_3$ and $4.5J_1 = 36J_3 = K_1 = 81K_3$, shown in the left and right insets respectively, the symmetric bicritical point P_4 is replaced, respectively, by tricritical points R_3 and R_1 and critical endpoints L_1 and L_3 in asymmetric phase diagrams.

tent with the corresponding zero-temperature phase diagram, in the right panel of Fig. 2.

IV. 4-STATE POTTS SUBSPACE

Returning to the most general spin-3/2 Ising Hamiltonian in Eq.(2), for

$$4J_1 = 36J_3 = K_1 = 81K_3, \quad J_{13} = K_{13} = \Delta = 0, \quad (6)$$

the model reduces to the 4-state Potts model, with Hamiltonian

$$-\beta\mathcal{H} = \frac{J_1}{2} \sum_{\langle ij \rangle} \delta(s_i, s_j), \quad (7)$$

where the Kronecker delta function is $\delta(s_i, s_j) = 1(0)$ for $s_i = s_j (s_i \neq s_j)$.

Figure 5 gives the calculated phase diagram in temperature $1/J_1$ and chemical potential Δ/J_1 , for the 4-state Potts side conditions $4J_1 = 36J_3 = K_1 = 81K_3$, $J_{13} = K_{13} = 0$. In this figure, $\Delta/J_1 = 0$ is the 4-state Potts

subspace, where the system is permutation symmetric with respect to the 4 states $s_i = \pm 3/2, \pm 1/2$. Varying Δ/J_1 from zero gives the "symmetric bicritical" phase diagram around the Potts multicritical point. This phase diagram is exact for the $d = 3$ hierarchical lattice, but approximate for the cubic lattice. For the cubic lattice, from 3-state Potts model analogy [95], we expect short first-order segments on each phase boundary leading to the 4-state Potts transition, which occurs as first-order with 5-phase coexistence. In renormalization-group theory, this first-order behavior is revealed by the accounting of local disorder as effective vacancies [74, 75]. For the spin-3/2 Ising model, the resulting renormalization-group flows would be in the space of the spin-2 Ising model. In Fig. 5, for $3.5J_1 = 36J_3 = K_1 = 81K_3$ and $4.5J_1 = 36J_3 = K_1 = 81K_3$, shown in the left and right insets respectively, the symmetric Potts transition point P_4 is replaced, respectively, by tricritical points R_3 and R_1 and critical endpoints L_1 and L_3 in asymmetric phase diagrams.

V. CONCLUSION

We have obtained the full unified global phase diagram of the spin-3/2 Ising model in $d = 3$, deriving extremely rich structures and fully showing the logical continuity among these complicated structures. Thus, renormalization-group theory reveals eight different orientationally and/or positionally ordered and disordered phases; first- and second-order phase transitions; double critical points, first-order and critical lines between ordered phases, critical endpoints, usual and unexpected (inverted) bicritical points, tricritical points, different tetracritical points, very high (quintuple) phase boundary reentrances, and zero-temperature criticality and bicriticality. Fourteen different phase diagram topologies, in the temperature and chemical potential variables, are presented here. The renormalization-group flows yielding this multicritical, multistructural global phase diagram are governed by 40 different fixed points (Table I). Globally distant in flow space, redundant fixed points nevertheless conserve the universality of critical exponents. The imbedding of the 4-state Potts symmetric subspace and phase transition is made explicit.

Acknowledgments

We thank Tolga Çağlar for his help. Support by the Alexander von Humboldt Foundation, the Scientific and Technological Research Council of Turkey (TÜBİTAK), and the Academy of Sciences of Turkey (TÜBA) is gratefully acknowledged.

-
- [1] M. Blume, V. J. Emery, and R. B. Griffiths, *Phys. Rev. A* **4**, 1071 (1971).
- [2] A. N. Berker and M. Wortis, *Phys. Rev. B* **14**, 4946 (1976).
- [3] W. Hoston and A. N. Berker, *Phys. Rev. Lett.* **67**, 1027 (1991).
- [4] J. Sivardière, A. N. Berker, and M. Wortis, *Phys. Rev. B* **7**, 343 (1973).
- [5] S. Krinsky and D. Mukamel, *Phys. Rev. B* **11**, 399 (1975).
- [6] S. Krinsky and D. Mukamel, *Phys. Rev. B* **12**, 211 (1975).
- [7] A. Bakchich, A. Bassir, and A. Benyoussef, *Physica A* **195**, 188 (1993).
- [8] A. Bakchich, S. Bekhechi, and A. Benyoussef, *Physica A* **210**, 415 (1994).
- [9] N. Sh. Izmailian and N. S. Ananikian, *Phys. Rev. B* **50**, 6829 (1994).
- [10] S. Bekhechi and A. Benyoussef, *Phys. Rev. B* **56**, 13954 (1997).
- [11] J. C. Xavier, F. C. Alcaraz, D. Peña Lara, and J. A. Plascak, *Phys. Rev. B* **57**, 11575 (1998).
- [12] E. Albayrak and M. Keskin, *J. Mag. Mag. Mat.* **218**, 121 (2000).
- [13] A. Bakchich and M. El Bouziani, *J. Phys. Condens. Matter* **13**, 91 (2001).
- [14] A. Bakchich and M. El Bouziani, *Phys. Rev. B* **63**, 064408 (2001).
- [15] O. Özsoy, E. Albayrak, and M. Keskin, *Physica A* **304**, 443 (2002).
- [16] E. Albayrak and M. Keskin, *J. Mag. Mag. Mat.* **241**, 249 (2002).
- [17] C. Ekiz, E. Albayrak, and M. Keskin, *J. Mag. Mag. Mat.* **256**, 311 (2003).
- [18] O. Özsoy and M. Keskin, *Physica A* **319**, 404 (2003).
- [19] O. Canko and M. Keskin, *Phys. Lett. A* **320**, 22 (2003).
- [20] J. A. Plascak and D. P. Landau, *Phys. Rev. E* **67**, 015103R (2003).
- [21] O. Canko and M. Keskin, *Phys. Lett. A* **348**, 9 (2005).
- [22] O. Canko and M. Keskin, *Int. J. Mod. Phys.* **20**, 455 (2006).
- [23] O. Canko and M. Keskin, *Physica A* **363**, 315 (2006).
- [24] O. Canko, B. Deviren, and M. Keskin, *J. Phys. - Cond. Mat.* **18**, 6635 (2006).
- [25] M. Keskin, M. A. Pinar, A. Erdinç, and O. Canko, *Physica A* **364**, 263 (2006).
- [26] M. Keskin, M. A. Pinar, A. Erdinç, and O. Canko, *Phys. Lett. A* **353**, 116 (2006).
- [27] M. Keskin, O. Canko, and B. Deviren, *Phys. Rev. E* **74**, 011110 (2006).
- [28] M. Keskin, O. Canko, and M. Kirak, *J. Stat. Phys.* **127**, 359 (2007).
- [29] M. El Bouziani and A. Gaye, *Physica A* **392**, 2643 (2013).
- [30] A. A. Migdal, *Zh. Eksp. Teor. Fiz.* **69**, 1457 (1975) [*Sov. Phys. JETP* **42**, 743 (1976)].
- [31] L. P. Kadanoff, *Ann. Phys. (N.Y.)* **100**, 359 (1976).
- [32] A. N. Berker and S. Ostlund, *J. Phys. C* **12**, 4961 (1979).
- [33] R. B. Griffiths and M. Kaufman, *Phys. Rev. B* **26**, 5022R (1982).
- [34] M. Kaufman and R. B. Griffiths, *Phys. Rev. B* **30**, 244 (1984).
- [35] S. R. McKay and A. N. Berker, *Phys. Rev. B* **29**, 1315 (1984).
- [36] A. N. Berker and S. R. McKay, *J. Stat. Phys.* **36**, 787 (1984).
- [37] M. Hinczewski and A. N. Berker, *Phys. Rev. E* **73**, 066126 (2006).
- [38] M. Kaufman and H. T. Diep, *Phys. Rev. E* **84**, 051106 (2011).
- [39] M. Kotorowicz and Y. Kozitsky, *Cond. Matter Phys.* **14**, 13801 (2011).
- [40] J. Barre, *J. Stat. Phys.* **146**, 359 (2012).
- [41] C. Monthus and T. Garel, *J. Stat. Mech. - Theory and Experiment*, P05002 (2012).
- [42] Z. Z. Zhang, Y. B. Sheng, Z. Y. Hu, and G. R. Chen, *Chaos* **22**, 043129 (2012).
- [43] S.-C. Chang and R. Shrock, *Phys. Lett. A* **377**, 671 (2013).
- [44] Y.-L. Xu, L.-S. Wang, and X.-M. Kong, *Phys. Rev. A* **87**, 012312 (2013).
- [45] S. Hwang, D.-S. Lee, and B. Kahng, *Phys. Rev. E* **87**, 022816 (2013).
- [46] E. Ilker and A. N. Berker, *Phys. Rev. E* **87**, 032124 (2013).
- [47] R. F. S. Andrade and H. J. Herrmann, *Phys. Rev. E* **87**, 042113 (2013).
- [48] R. F. S. Andrade and H. J. Herrmann, *Phys. Rev. E* **88**, 042122 (2013).
- [49] C. Monthus and T. Garel, *J. Stat. Phys. - Theory and Experiment*, P06007 (2013).
- [50] O. Melchert and A. K. Hartmann, *Eur. Phys. J. B* **86**, 323 (2013).
- [51] J.-Y. Fortin, *J. Phys.-Condensed Matter* **25**, 296004 (2013).
- [52] Y. H. Wu, X. Li, Z. Z. Zhang, and Z. H. Rong, *Chaos Solitons Fractals* **56**, 91 (2013).
- [53] P. N. Timonin, *Low Temp. Phys.* **40**, 36 (2014).
- [54] B. Derrida and G. Giacomin, *J. Stat. Phys.* **154**, 286 (2014).
- [55] M. F. Thorpe and R. B. Stinchcombe, *Philos. Trans. Royal Soc. A - Math. Phys. Eng. Sciences* **372**, 20120038 (2014).
- [56] A. Efrat and M. Schwartz, *Physica A* **414**, 137 (2014).
- [57] C. Monthus and T. Garel, *Phys. Rev. B* **89**, 184408 (2014).
- [58] T. Nogawa and T. Hasegawa, *Phys. Rev. E* **89**, 042803 (2014).
- [59] M. L. Lyra, F. A. B. F. de Moura, I. N. de Oliveira, and M. Serva, *Phys. Rev. E* **89**, 052133 (2014).
- [60] V. Singh and S. Boettcher, *Phys. Rev. E* **90**, 012117 (2014).
- [61] Y.-L. Xu, X. Zhang, Z.-Q. Liu, K. Xiang-Mu, and R. Ting-Qi, *Eur. Phys. J. B* **87**, 132 (2014).
- [62] Y. Hirose, A. Oguchi, and Y. Fukumoto, *J. Phys. Soc. Japan* **83**, 074716 (2014).
- [63] E. Ilker and A. N. Berker, *Phys. Rev. E* **89**, 042139 (2014).
- [64] V. S. T. Silva, R. F. S. Andrade, and S. R. Salinas, *Phys. Rev. E* **90**, 052112 (2014).
- [65] Y. Hotta, *Phys. Rev. E* **90**, 052821 (2014).
- [66] E. Ilker and A. N. Berker, *Phys. Rev. E* **90**, 062112 (2014).
- [67] S. Boettcher, S. Falkner, and R. Portugal, *Phys. Rev. A* **91** 052330 (2015).

- [68] M. Demirtaş, A. Tuncer, and A. N. Berker, *Phys. Rev. E* **92**, 022136 (2015).
- [69] S. Boettcher and C. T. Brunson, *Eur. Phys. Lett.* **110**, 26005 (2015).
- [70] Y. Hirose, A. Ogushi, and Y. Fukumoto, *J. Phys. Soc. Japan* **84**, 104705 (2015).
- [71] S. Boettcher and L. Shanshan, *J. Phys. A* **48**, 415001 (2015).
- [72] A. Nandy and A. Chakrabarti, *Phys. Lett.* **379**, 2876 (2015).
- [73] A. N. Berker, *Phys. Rev. B* **12**, 2752 (1975).
- [74] B. Nienhuis, A. N. Berker, E. K. Riedel, and M. Schick, *Phys. Rev. Lett.* **43**, 737 (1979).
- [75] D. Andelman and A. N. Berker, *J. Phys. A* **14**, L91 (1981).
- [76] A. N. Berker and L. P. Kadanoff, *J. Phys. A* **13**, 1469 (1980).
- [77] A. N. Berker and L. P. Kadanoff, *J. Phys. A* **13**, 3786 (1980).
- [78] A. N. Berker, S. Ostlund, and F. A. Putnam, *Phys. Rev. B* **17**, 3650 (1978).
- [79] A. N. Berker and D. R. Nelson, *Phys. Rev. B* **19**, 2488 (1979).
- [80] J. O. Indekeu and A. N. Berker, *Physica A* **140**, 368 (1986).
- [81] J. O. Indekeu, A. N. Berker, C. Chiang, and C. W. Garland, *Phys. Rev. A* **35**, 1371 (1987).
- [82] S. R. McKay, A. N. Berker, and S. Kirkpatrick, *Phys. Rev. Lett.* **48**, 767 (1982).
- [83] A. Falicov, A. N. Berker, and S. R. McKay, *Phys. Rev. B* **51**, 8266 (1995).
- [84] K. Hui and A. N. Berker, *Phys. Rev. Lett.* **62**, 2507 (1989); erratum **63**, 2433 (1989).
- [85] M. Hinczewski and A. N. Berker, *Phys. Rev. B* **78**, 064507 (2008).
- [86] F. J. Wegner, *J. Phys. C* **7**, 2098 (1974).
- [87] J. A. Pople and F. E. Karasz, *J. Phys. Chem. Solids* **18**, 28 (1961).
- [88] P. E. Cladis, *Phys. Rev. Lett.* **35**, 48 (1975).
- [89] F. Hardouin, A. M. Levelut, M. F. Achard, and G. Sigaud, *J. Chim. Phys.* **80**, 53 (1983).
- [90] R. R. Netz and A. N. Berker, *Phys. Rev. Lett.* **68**, 333 (1992).
- [91] S. Kumari and S. Singh, *Phase Transitions* **88**, 1225 (2015).
- [92] R. G. Caflisch, A. N. Berker, and M. Kardar, *Phys. Rev. B* **31**, 4527 (1985).
- [93] A. Falicov and A. N. Berker, *Phys. Rev. B* **51**, 12458 (1995).
- [94] A. D. Bruce and A. Aharony, *Phys. Rev. B* **11**, 478 (1975).
- [95] J. P. Straley and M. E. Fisher, *J. Phys. A* **6**, 1310 (1973).

I. Stable Fixed Points: Phase Sinks

F_3 Long Ferro $\begin{pmatrix} 1 & 0 & 0 & 0 \\ 0 & 0 & 0 & 0 \\ 0 & 0 & 0 & 0 \\ 0 & 0 & 0 & 1 \end{pmatrix}$	F_1 Short Ferro $\begin{pmatrix} 0 & 0 & 0 & 0 \\ 0 & 1 & 0 & 0 \\ 0 & 0 & 1 & 0 \\ 0 & 0 & 0 & 0 \end{pmatrix}$	A_3 Long Antiferro $\begin{pmatrix} 0 & 0 & 0 & 1 \\ 0 & 0 & 0 & 0 \\ 0 & 0 & 0 & 0 \\ 1 & 0 & 0 & 0 \end{pmatrix}$	A_1 Short Antiferro $\begin{pmatrix} 0 & 0 & 0 & 0 \\ 0 & 0 & 1 & 0 \\ 0 & 1 & 0 & 0 \\ 0 & 0 & 0 & 0 \end{pmatrix}$
F_{13} Mixed Ferro $\begin{pmatrix} 0 & 1 & 0 & 0 \\ 1 & 0 & 0 & 0 \\ 0 & 0 & 0 & 1 \\ 0 & 0 & 1 & 0 \end{pmatrix}$	A_q Plastic Crystal $\begin{pmatrix} 0 & 1 & 1 & 0 \\ 1 & 0 & 0 & 1 \\ 1 & 0 & 0 & 1 \\ 0 & 1 & 1 & 0 \end{pmatrix}$	D_3 Long Disordered $\begin{pmatrix} 1 & 0 & 0 & 1 \\ 0 & 0 & 0 & 0 \\ 0 & 0 & 0 & 0 \\ 1 & 0 & 0 & 1 \end{pmatrix}$	D_1 Short Disordered $\begin{pmatrix} 0 & 0 & 0 & 0 \\ 0 & 1 & 1 & 0 \\ 0 & 1 & 1 & 0 \\ 0 & 0 & 0 & 0 \end{pmatrix}$

II. Singly Unstable Fixed Points: Attractors of Second-Order Phase Boundaries and their Relevant Exponent y_T

$F_3 - D_3$ $y_T = 0.9260$ $\begin{pmatrix} 1 & 0 & 0 & t \\ 0 & 0 & 0 & 0 \\ 0 & 0 & 0 & 0 \\ t & 0 & 0 & 1 \end{pmatrix}$	$F_1 - D_1$ $y_T = 0.9260$ $\begin{pmatrix} 0 & 0 & 0 & 0 \\ 0 & 1 & t & 0 \\ 0 & t & 1 & 0 \\ 0 & 0 & 0 & 0 \end{pmatrix}$	$F_{13} - A_q$ $y_T = 0.9260$ $\begin{pmatrix} 0 & 1 & t & 0 \\ 1 & 0 & 0 & t \\ t & 0 & 0 & 1 \\ 0 & t & 1 & 0 \end{pmatrix}$	$A_3 - D_3$ $y_T = 0.9260$ $\begin{pmatrix} t & 0 & 0 & 1 \\ 0 & 0 & 0 & 0 \\ 0 & 0 & 0 & 0 \\ 1 & 0 & 0 & t \end{pmatrix}$	$A_1 - D_1$ $y_T = 0.9260$ $\begin{pmatrix} 0 & 0 & 0 & 0 \\ 0 & t & 1 & 0 \\ 0 & 1 & t & 0 \\ 0 & 0 & 0 & 0 \end{pmatrix}$
$F_3 - F_{13}$ $y_T = 1.8104$ $\begin{pmatrix} v & 1 & 0 & 0 \\ 1 & w & 0 & 0 \\ 0 & 0 & w & 1 \\ 0 & 0 & 1 & v \end{pmatrix}$	$F_{13} - F_1$ $y_T = 1.8104$ $\begin{pmatrix} w & 1 & 0 & 0 \\ 1 & v & 0 & 0 \\ 0 & 0 & v & 1 \\ 0 & 0 & 1 & w \end{pmatrix}$	$D_3 - A_q$ $y_T = 1.8104$ $\begin{pmatrix} v & 1 & 1 & v \\ 1 & w & w & 1 \\ 1 & w & w & 1 \\ v & 1 & 1 & v \end{pmatrix}$	$A_q - D_1$ $y_T = 1.8104$ $\begin{pmatrix} w & 1 & 1 & w \\ 1 & v & v & 1 \\ 1 & v & v & 1 \\ w & 1 & 1 & w \end{pmatrix}$	

III. Singly Unstable Fixed Points: Attractors of First-Order Phase Boundaries with Relevant Exponent $y_T = d$

$F_3 - F_1$ $y_T = d$ $\begin{pmatrix} 1 & 0 & 0 & 0 \\ 0 & 1 & 0 & 0 \\ 0 & 0 & 1 & 0 \\ 0 & 0 & 0 & 1 \end{pmatrix}$	$D_3 - D_1$ $y_T = d$ $\begin{pmatrix} 1 & 0 & 0 & 1 \\ 0 & 1 & 1 & 0 \\ 0 & 1 & 1 & 0 \\ 1 & 0 & 0 & 1 \end{pmatrix}$	$F_3 - D_1$ $y_T = d$ $\begin{pmatrix} 1 & 0 & 0 & 0 \\ 0 & u & u & 0 \\ 0 & u & u & 0 \\ 0 & 0 & 0 & 1 \end{pmatrix}$	$F_1 - D_3$ $y_T = d$ $\begin{pmatrix} u & 0 & 0 & u \\ 0 & 1 & 0 & 0 \\ 0 & 0 & 1 & 0 \\ u & 0 & 0 & u \end{pmatrix}$
--	--	--	--

IV. Singly Unstable Fixed Points: Attractors of Smooth Continuation (Null) Lines

$F_3 - F_1$ $\begin{pmatrix} 1 & 1 & 0 & 0 \\ 1 & 1 & 0 & 0 \\ 0 & 0 & 1 & 1 \\ 0 & 0 & 1 & 1 \end{pmatrix}$	$D_3 - D_1$ $\begin{pmatrix} 1 & 1 & 1 & 1 \\ 1 & 1 & 1 & 1 \\ 1 & 1 & 1 & 1 \\ 1 & 1 & 1 & 1 \end{pmatrix}$
---	---

V. Multiply Unstable Fixed Points: Attractors of Multicritical Points and their Leading 2 Relevant Exponents y_{T1}, y_{T2}

L_1 Critical Endpoint $y_{T1} = d, y_{T2} = 0.9260$ $\begin{pmatrix} 1.0212 & 0 & 0 & 0 \\ 0 & 1 & t & 0 \\ 0 & t & 1 & 0 \\ 0 & 0 & 0 & 1.0212 \end{pmatrix}$	L_3 Critical Endpoint $y_{T1} = d, y_{T2} = 0.9260$ $\begin{pmatrix} 1 & 0 & 0 & t \\ 0 & 1.0212 & 0 & 0 \\ 0 & 0 & 1.0212 & 0 \\ t & 0 & 0 & 1 \end{pmatrix}$	B Bicritical $y_{T1} = 2.4649, y_{T2} = 1.0000$ $\begin{pmatrix} 0.3347 & 1 & 0.3347 & 1 \\ 1 & 1 & 0.3347 & 0.3347 \\ 0.3347 & 0.3347 & 1 & 1 \\ 1 & 0.3347 & 1 & 0.3347 \end{pmatrix}$
R_1 Tricritical $y_{T1} = 2.1733, y_{T2} = 0.7352$ $\begin{pmatrix} 0.9474 & 0.9316 & 0.9316 & 0.9474 \\ 0.9316 & 1 & 0.8344 & 0.9316 \\ 0.9316 & 0.8344 & 1 & 0.9316 \\ 0.9474 & 0.9316 & 0.9316 & 0.9474 \end{pmatrix}$	R_3 Tricritical $y_{T1} = 2.1733, y_{T2} = 0.7352$ $\begin{pmatrix} 1 & 0.9316 & 0.9316 & 0.8344 \\ 0.9316 & 0.9474 & 0.9474 & 0.9316 \\ 0.9316 & 0.9474 & 0.9474 & 0.9316 \\ 0.8344 & 0.9316 & 0.9316 & 1 \end{pmatrix}$	P_4 4-Potts $y_{T1} = 2.5434, y_{T2} = 1.0667$ $\begin{pmatrix} 1 & 0.8926 & 0.8926 & 0.8926 \\ 0.8926 & 1 & 0.8926 & 0.8926 \\ 0.8926 & 0.8926 & 1 & 0.8926 \\ 0.8926 & 0.8926 & 0.8926 & 1 \end{pmatrix}$
M_1 Tetracritical $y_{T1} = 1.8104, y_{T2} = 0.9260$ $\begin{pmatrix} 0.4099 & 1 & 0.9243 & 0.3789 \\ 1 & 0.9300 & 0.8596 & 0.9243 \\ 0.9243 & 0.8596 & 0.9300 & 1 \\ 0.3789 & 0.9243 & 1 & 0.4099 \end{pmatrix}$	M_3 Tetracritical $y_{T1} = 1.8104, y_{T2} = 0.9260$ $\begin{pmatrix} 0.9300 & 1 & 0.9243 & 0.8596 \\ 1 & 0.4099 & 0.3789 & 0.9243 \\ 0.9243 & 0.3789 & 0.4099 & 1 \\ 0.8596 & 0.9243 & 1 & 0.9300 \end{pmatrix}$	N_1 Tetracritical $y_{T1} = 2.0000, y_{T2} = 1.6805$ $\begin{pmatrix} 0.3228 & 1 & 0.2960 & 0.3228 \\ 1 & 0.9170 & 0.9170 & 0.2960 \\ 0.2960 & 0.9170 & 0.9170 & 1 \\ 0.3228 & 0.2960 & 1 & 0.3228 \end{pmatrix}$
N_3 Tetracritical $y_{T1} = 2.0000, y_{T2} = 1.6805$ $\begin{pmatrix} 0.9170 & 1 & 0.2960 & 0.9170 \\ 1 & 0.3228 & 0.3228 & 0.2960 \\ 0.2960 & 0.3228 & 0.3228 & 1 \\ 0.9170 & 0.2960 & 1 & 0.9170 \end{pmatrix}$	I Interceding $y_{T1} = 2.5732, y_{T2} = 0.9260$ $\begin{pmatrix} 1 & 0.8543 & t & t \\ 0.8543 & 1 & t & t \\ t & t & 1 & 0.8543 \\ t & t & 0.8543 & 1 \end{pmatrix}$	I_{13} and I_A Interceding $y_{T1} = 1.4268, y_{T2} = 0.9260$ $\begin{pmatrix} t & 1 & 0 & 0 \\ 1 & t & 0 & 0 \\ 0 & 0 & t & 1 \\ 0 & 0 & 1 & t \end{pmatrix}$ and $\begin{pmatrix} t & 1 & 1 & t \\ 1 & t & t & 1 \\ 1 & t & t & 1 \\ t & 1 & 1 & t \end{pmatrix}$

TABLE I: Fixed points underpinning the renormalization-group flows determining the global phase diagram of the $s = 3/2$ Ising model. In this Table, the matrix elements are $t = 0.9243, u = 0.9481, v = 0.9300, w = 0.4099$. The fixed point for the isolated critical point in Fig. 1(a) has thermal exponent $y_T = 0.9260$ along the first-order transition direction and magnetic